remote sensing

MDPI

Technical Note

Optimising the Complex Refractive Index Model for Estimating the Permittivity of Heterogeneous Concrete Models

Hossain Zadhoush [1,*], Antonios Giannopoulos [1] and Iraklis Giannakis [2]

[1] School of Engineering, Institute for Infrastructure and Environment, The University of Edinburgh, Edinburgh EH8 9YL, UK; A.Giannopoulos@ed.ac.uk
[2] School of Geosciences, University of Aberdeen, Aberdeen AB24 3UE, UK; Iraklis.Giannakis@abdn.ac.uk
* Correspondence: h.zadhoush@ed.ac.uk

Abstract: Estimating the permittivity of heterogeneous mixtures based on the permittivity of their components is of high importance with many applications in ground penetrating radar (GPR) and in electrodynamics-based sensing in general. Complex Refractive Index Model (CRIM) is the most mainstream approach for estimating the bulk permittivity of heterogeneous materials and has been widely applied for GPR applications. The popularity of CRIM is primarily based on its simplicity while its accuracy has never been rigorously tested. In the current study, an optimised shape factor is derived that is fine-tuned for modelling the dielectric properties of concrete. The bulk permittivity of concrete is expressed with respect to its components i.e., aggregate particles, cement particles, air-voids and volumetric water fraction. Different combinations of the above materials are accurately modelled using the Finite-Difference Time-Domain (FDTD) method. The numerically estimated bulk permittivity is then used to fine-tune the shape factor of the CRIM model. Then, using laboratory measurements it is shown that the revised CRIM model over-performs the default shape factor and provides with more accurate estimations of the bulk permittivity of concrete.

Keywords: GPR; FDTD; antenna; time-zero; permittivity measurement; gprMax; NDT; concrete; CRIM model; shape factor; GPU

Citation: Zadhoush, H.; Giannopoulos, A.; Giannakis, I. Optimising the Complex Refractive Index Model for Estimating the Permittivity of Heterogeneous Concrete Models. *Remote Sens.* **2021**, *13*, 723. https://doi.org/10.3390/rs13040723

Academic Editor: Mercedes Solla
Received: 17 December 2020
Accepted: 10 February 2021
Published: 16 February 2021

1. Introduction

Ground penetrating radar (GPR) is a non-destructive geophysical technique which has a wide range of applications [1–3] and it is extensively used for civil engineering. It is used for surveying buried utilities [4,5] , roads [6,7], tunnels [8], bridges [9–11] and concrete [12,13]. It is also used for detecting landmines [14], concrete steel bars [15], moisture clusters [16] and air voids in asphalt [17,18]. GPR is an electromagnetic investigative tool which it has been around for many years but GPR modelling is rapidly becoming increasingly useful and the quality of GPR models is becoming more realistic [1].

One of the most important applications of GPR is monitoring and condition assessment of concrete structures. Investigations that usually take place for GPR applications involve shallow-depth buried targets or ones that are located close to the surface. For instance, such applications are detecting the location of rebars, air voids, moisture content and cracks [19]. For concrete construction, many mixtures exist with a variety of content combinations dependant on the application. These mixtures have various material percentages for aggregate, cement and sand which can result in a different dielectric constant of the resulting concrete product. Concrete is a heterogeneous material and the calculation of the dielectric constant has been the interest of many researchers [20–22]. When analysing GPR data, having the wrong estimation of the dielectric properties will result in an incorrect interpretation of key parameters that will be extracted from them. These parameters are the GPR wave velocity in the mixture which is used to convert its two-way travel time in depth, and also, the moisture content. So, if the dielectric constant is not estimated correctly, the GPR analysis of the data will be wrong and problematic. Therefore, in order to

investigate the electrical properties of concrete, the dielectric constant should be calculated accurately [23,24]. There are many methodologies that have been used in the past for this purpose which raises an issue concerning which method is the most effective for estimating the bulk permittivity of concrete mixtures.

Over the years many methods have been developed to estimate the bulk permittivity of heterogeneous materials [25,26]. The most common methods [27] are based on the Complex Refractive Index Model (CRIM) model [28], the Rayleigh model [29], the Böttcher model [30], the Brown model [31], the Wagner model [32], the Bruggeman model [33] and the Topp model [34]. These models calculate the dielectric constant of the mixture with respect to the dielectric properties and the volumetric fractions of its components. From the aforementioned models, CRIM has been established as the mainstream methodology in the GPR community mainly due to its simplicity and its straightforward implementation.

In this study, the CRIM mixing model was investigated in detail focusing on the key geometric parameter of the model. A methodology is presented in order to investigate the shape factor further and evaluate different estimates of it. This allows to determine the best shape factor and present a fine-tuned value for concrete structures. Our approach is based on numerical-synthetic experiments executed using gprMax [35,36] an open source electromagnetic solver using finite difference time domain method (FDTD) [37,38]. FDTD is robust, accurate, flexible, computationally efficient and uses time domain discretisation which is ideal for GPR scenarios [39–41]. As computational resources have improved and become more accessible, an increase in the knowledge and effectiveness of GPR modelling has been observed [42]. One of the advantages of GPR numerical modelling is that it is able to produce models that are close to reality and support research effort when restrictions exist to execute it physically. Numerical modelling has been widely used for designing various models and optimising complex antennas [43–45]. FDTD has been widely used to simulate different antenna models such as bowties [46–48], dipoles [49–52] and horn antennas [53,54]. In this study, the antenna used for the simulations was a model-equivalent of a GSSI 1.5 GHz centre frequency antenna structure available for experimentation [45,55].

Numerous realistic concrete models were simulated using an automatic framework that generates different distribution of aggregate particles, cement, air-voids and moisture content. The chloride content within the concrete is negligible thus the effects are not noticeable and were not considered in the numerical experiments [56,57] . The moisture content is a very important aspect and has been shown that greatly affects the overall dielectric properties of the concrete mixture [58,59]. It has been reported that moisture content greater than 5% has an important influence on the transmitted signal travelling through the concrete [60]. Therefore, in the current study, different mixtures with various degrees of moisture content have been numerically simulated and tested. In another framework, different mixtures with constituent variations have been tested and have shown minor effects on the permittivity in comparison with the moisture content, air-voids, cement and aggregate particles [61].

Using the aforementioned numerical framework, a coherent set of synthetic examples was generated. The synthetic set was subsequently used to fine-tune and optimise the shape factor such as the CRIM-based bulk permittivity to match the actual one. Using numerical experiments allowed to have full control on the volumetric fractions of the concrete's components. Thus, every term in the CRIM formula can be accurately implemented. The resulting optimised shape factor using the suggested scheme was evaluated in both synthetic and laboratory experiments indicating the validity and robustness of the revised CRIM model.

2. Methodology

CRIM (1) is one of the most used models by GPR practitioners for predicting the bulk permittivity of complex materials like concrete.

$$\varepsilon_b = \left(V_{ag} \varepsilon_{ag}^{\alpha} + V_a \varepsilon_a^{\alpha} + V_c \varepsilon_c^{\alpha} + V_w \varepsilon_w^{\alpha} \right)^{1/\alpha} \quad (1)$$

where ε_b is the bulk permittivity of the concrete mixture, V_{ag} and ε_{ag} are the volume and relative permittivity of aggregate, V_a and ε_a are the volumetric fraction of air-voids and relative permittivity of free space, V_c and ε_c are the volumetric fraction and relative permittivity of cement, V_m and ε_m are the volumetric fraction and relative permittivity of the moisture content and α is the shape factor.

The most common shape factor of CRIM model is usually $\alpha = 0.5$. This study investigates the CRIM formula in order to find an optimised shape factor for this specific problem. To be able to take this matter further, a training set needs to be built and to have control over this, numerical modelling was used.

Numerical modelling is a great tool when it comes to optimisation. In order to find the optimum shape factor, we used synthetic data to define the shape factor. After creating and simulating heterogeneous concrete models, a reflection from a Perfect Electric Conductor (PEC) target was used to predict the velocity and calculate the bulk permittivity. In order to achieve this, GPR data should be accurately picked regarding the time-zero position.

2.1. Time-zero

GPR applications requires great accuracy and precision. Such cases are when trying to locate gas pipes [62], for landmine detection [63] or concrete inspection [64] where it is necessary to position the time-zero accurately. Defining the exact location of time-zero on a GPR trace is still an open issue with no specific conclusive solution and usually addressed by taking into account the GPR manufacturers recommendations [65].

In Yelf's paper [65], a number of positions have been discussed as possible candidates for picking the time-zero for a GPR trace, such as the positive peak, negative peak, mid-amplitude point, and the first break position of the direct wave wavelet. Additionally, for the arrival time of the target's response, there are a number of possible positions that can be considered for calculating the two-way travel time. All of these cases have been considered and compared resulting in a better time-zero position. In this paper, the time-zero was positioned on the first peak of the direct wave and two way travel time was calculated from the time arrival average where the three reflected peaks of the target occur [66]. Figure 1 presents a GPR trace with a reflection from a PEC target. This time-zero picking methodology has been successfully evaluated using numerous numerical scenarios indicating the validity of the current approach.

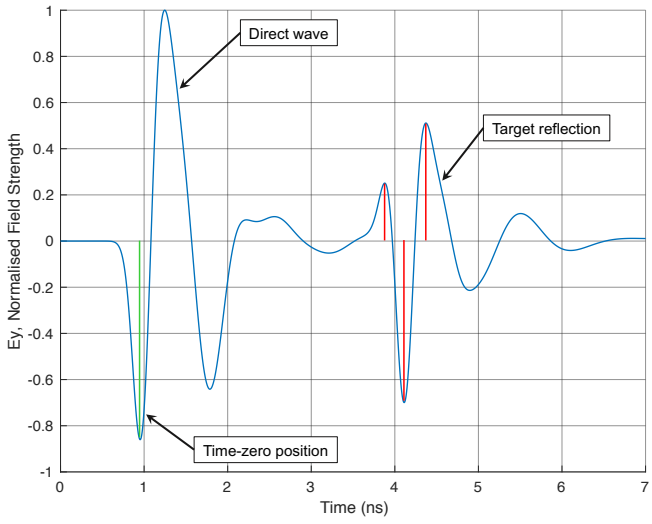

Figure 1. Time-zero is positioned on the first peak of the direct wave (green line). The two way travel time is calculated from the time-zero position to the average time of the three peaks (Perfect Electric Conductor (PEC) target response—red lines).

2.2. Concrete Modelling

The initial investigation of the CRIM model was performed based on a numerical homogeneous two dimensional (2D) model with a simple theoretical excitation source. The simulation showed promising results for the permittivity estimation of the concrete. In other words, the real and the estimated permittivities using CRIM were close. This provided confidence to upgrade the framework and design models which are much closer to reality. To increase the complexity of the model and be more realistic, a three dimensional (3D) concrete model was created including a realistic GSSI-like antenna.

Aggregates come in different distribution types, shapes and forms. In reality, aggregates do not overlap or collide with each other therefore, they were modelled in a non-overlapping environment. The disadvantage of this type of packing is that it is very time-consuming as it requires a long CPU run-time. This is because the aggregates need to find a position that does not collide or overlap with another aggregate. Simulating such models can take days or even weeks of run-time depending on the volume of spheres and the degree of compactness. The simulation results for both overlapping and non-overlapping aggregates were obtained and compared. The results were very similar and did not affect the outcomes of this study. Therefore, the numerical modelling was continued with overlapping aggregates as it required less computational run-time.

Another challenge for designing a realistic concrete model was the aggregate shape (random polygon shapes—rock). Numerical results showed a similar output despite the shape of the aggregate therefore, for this study, the type of aggregate used can be discarded. The rock aggregates come with some disadvantages. Firstly, it is very hard to calculate the volume of each aggregate hence not able to model a medium with a specific aggregate percentage. Secondly, much higher computational run-times are needed to produce the rock models thus it is very time-consuming when dealing with a large number of aggregates. Consequently, although the rock aggregate model displays a more realistic concrete mixture, taking into account the limitations and the fact that the results are similar to the sphere aggregates, in this study, the aggregates were kept as spheres and were randomly distributed with different diameters.

After establishing the aggregate shape the next step was to implement additional mixture content that exist in a concrete slab. As mentioned, concrete is a mixture of cement, aggregates, air-voids and moisture content. To add to the complexity of the model, air-voids and moisture particles are randomly distributed in the model in order to achieve a more realistic concrete structure. By changing the moisture or air-void percentages we can achieve different medium permittivities.

There are a limited number of studies that use realistic models due to their complexity and lack of available computational resources. The open-source GPU engine for gprMax has greatly accelerated the simulations. The simulations that are conducted using the GPU based gprMax solver are up to 30 times faster in comparison with the traditional CPU based one. CPU uses a few cores and is generally used for simple tasks whereas GPU works with thousands of efficient cores with a parallel architecture [36].

Figure 2 illustrates a heterogeneous concrete model with a size of 30 cm $\times$ 20 cm $\times$ 36 cm and a spatial discretisation of 1 mm. Aggregate, cement, air-voids and moisture content with different percentages were randomly distributed in order to achieve different concrete mixtures. A PEC plate was placed at the bottom of the model that resulted in a strong reflection which would be used later on to derive the bulk permittivity of the investigated medium. Each mixture was simulated and the reflected signals were processed to find the GPR wave propagation of velocity and therefore calculate the bulk permittivity. The GSSI-like 1.5 GHz centre frequency antenna structure was coupled to the concrete surface. This transducer consist of a transmitter/receiver (Tx/Rx) bowtie (copper) pair, printed circuit boards—PCBs (glass fiber), electromagnetic absorber (carbon-loaded foam), shield (PEC) and a red case (polypropylene) [67].

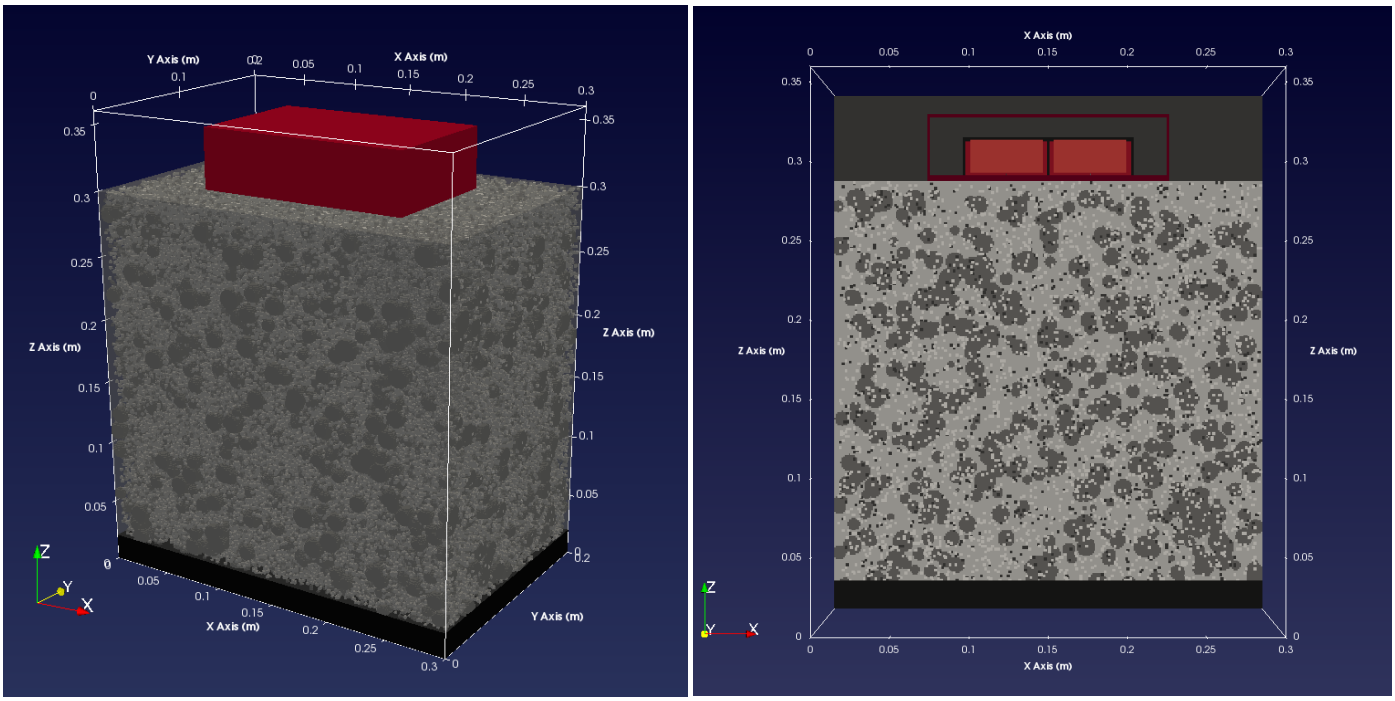

(**a**) Heterogeneous 3D concrete model (**b**) Slice of heterogeneous concrete model

Figure 2. Heterogeneous concrete model is plotted using Paraview [68]. The model employs a 1.5 GHz centre frequency GSSI-like antenna structure on top of the concrete. A PEC plate is placed below the concrete model in order to obtain a perfect reflection. The geometry dimension of the models is 30 cm × 20 cm × 36 cm. (**a**) 3D view of the concrete model. (**b**) A slice of the 3D model which allows for a better understanding of the material distribution.

Producing a realistic concrete model requires the material mixture to follow a rational percentage range. The permittivity of the materials used in the concrete mixture combinations with their corresponding percentage ranges are shown in Table 1. Notice that the imaginary is omitted from the simulations since in the current study we try to infer the permittivity from the bulk velocity which is not affected by electromagnetic losses. Numerous concrete mixtures were synthetically generated based on the percentages shown in Table 1. Various concretes with different aggregate, cement, air and water fraction percentages were investigated numerically in order to calculate their resulting bulk permittivity. Each concrete mixture was simulated multiple times to find the average permittivity as presented in Figure 3. The estimated bulk permittivity from the numerical modelling will be used in section 2.3 to calibrate the shape factor of the CRIM model and generate a better formula with a more accurate shape factor that can accurately predict the bulk permittivity of concrete mixtures based on its aggregate, cement, water and air fraction.

Table 1. The range of components used to generate the training data. Notice that the water is assumed to be bound and therefore its relaxation frequency is shifted to lower frequencies which results to a lower permittivity value for the frequency range of interest [69]. The percentages of the components are for on service concrete.

Material	Mixture Percentage	Permittivity (ε)
Aggregate	60–75%	7
Cement	7–15%	3
Air	1–8%	1
Water	14–21%	37.54 [69]

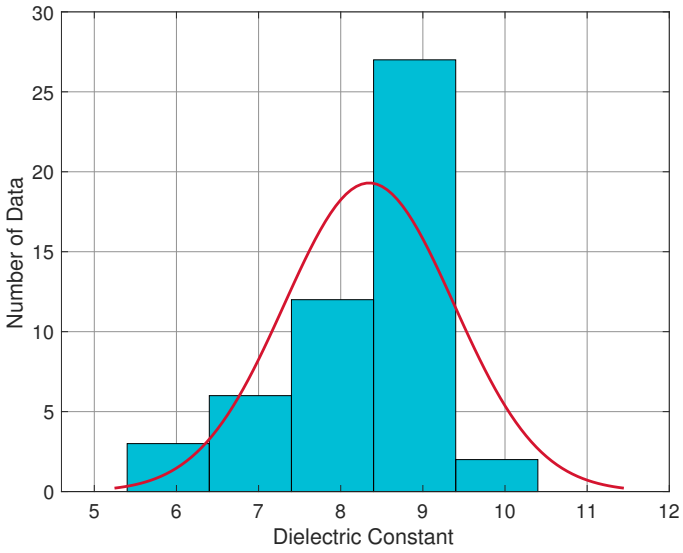

Figure 3. A random concrete model is simulated a number of times (×50) with different particle distributions in order to find its average bulk permittivity based on the reflection from the PEC reflector. This process neglects abnormal permittivity and allows the output to be more precise.

The PEC plate at the bottom of the model had a thickness of 2 cm. The GPR signals propagating through the medium did not transmit through the PEC and all of the energy from the impinging signals on the plate was reflected hence the thickness is not important. In reality, aggregates come in various shapes and sizes. To keep the numerical modelling as realistic as possible, different aggregate sizes were used. The size of the aggregates distributed in the mixture had a radius range from 4 to 8 mm [69,70] for coarse aggregates. As the aggregate percentage reached 60%, the radius was automatically decreased to a range of 1 to 2 mm [69,71] in order to simulate smaller or fine aggregates into the model and reach the specified percentage. This made the resulting shape factor tuned for an average size of particles and not for a specific one. Moisture and air-void particles were randomly distributed around the aggregates according to the selected percentage. The cement material was used as the background material. In other words, it filled up the remaining spaces of the concrete mixture. In regards to the water permittivity, there are two types of water. Bound and unbound (free) water. Bound water is a thin layer of water or moisture which surrounds mineral surfaces such as soil and concrete. Water has a strong electrical polarity hence it bounds very easily with other surfaces [72]. This has a high impact on the permittivity of the material which the water molecules bound with. The dielectric constant of bound water in comparison with free water (ε_r = 81) is much smaller. In a recent study, the permittivity of the liquid phase was fitted in a non-linear CRIM and permittivity of ε_r = 37.54 was calculated [69]. Figure 4 illustrates a set of concrete mixtures generated using the aforementioned procedure. The volumetric percentages of the components for each model are given in Table 2.

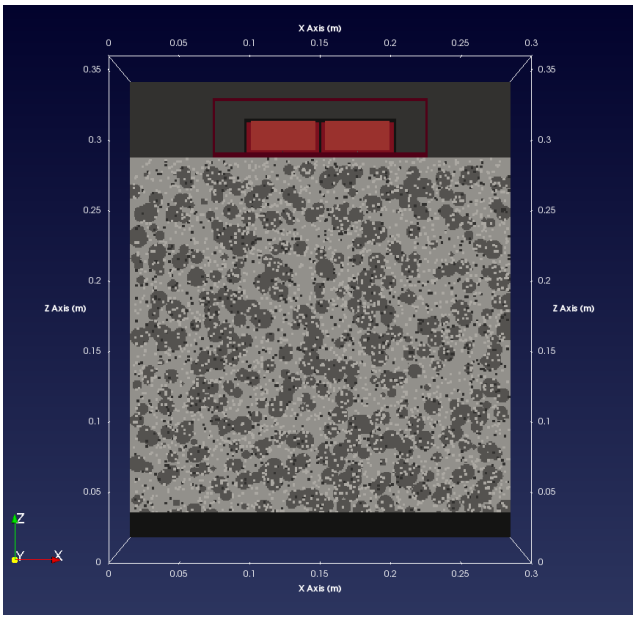

(**a**) Different distribution

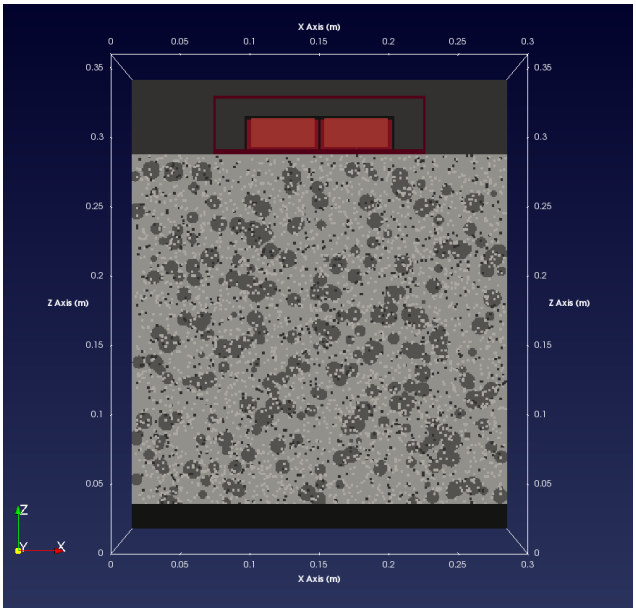

(**b**) Low aggregate mix

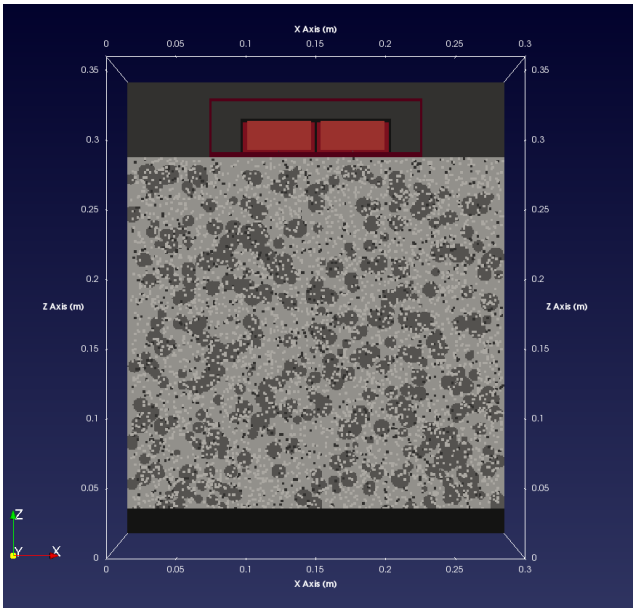

(**c**) High moisture mix

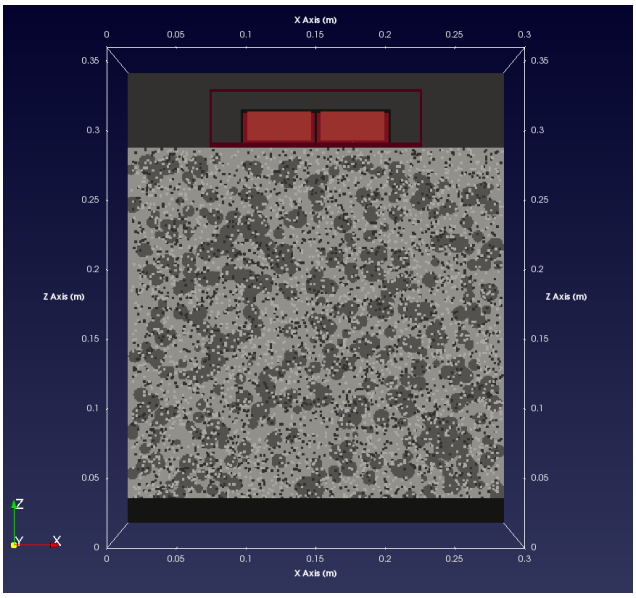

(**d**) High air-void mix

Figure 4. Heterogeneous concrete mix with different aggregates, air-voids and moisture content. (**a**) presents the same mixture content as (**b**) but with different distribution. (**b**) shows a mixture with low aggregate content. (**c**) illustrates high moisture content concrete resulting in a high permittivity. Finally, (**d**) indicates high air-void content allowing the GPR signal to travel with a higher velocity. 64 representative concrete mixtures were selected from the training pool and each one was simulated 50 times resulting in 3200 simulations. The red box corresponds to the numerical equivalent of the GSSI 1.5 GHz antenna structure. The volumetric percentages of the components for each model are shown in Table 2.

Table 2. The volumetric fraction of the concrete's components of the models shown in Figure 4. Some of these percentages are not within the ranges shown in table 1 in order to illustrate the modelling capabilities of the current framework for extreme cases.

Model	Aggregate	Cement	Air-Voids	Moisture Content
a	65%	15%	5%	15%
b	45%	27%	11%	17%
c	60%	14%	5%	21%
d	65%	10%	15%	10%

2.3. Optimisation and Comparison

A simple method that is used to estimate the bulk relative effective permittivity for complex mixtures such as heterogeneous concrete models is the CRIM model as presented in Equation (2)

$$\varepsilon_{mix} = \left(\sum_{i=1}^{N} f_i \varepsilon_i^{\alpha} \right)^{1/\alpha} \tag{2}$$

where ε_{mix} is the bulk permittivity of a mixture, f_i is the volume fraction of ith material, ε_i is the permittivity of the ith material, N is the number of phases and α is a constant that is usually set up to $\alpha = 1/2$. For concrete, Equation (2) becomes

$$\varepsilon_r^{\alpha} = V_{ag}\varepsilon_{ag}^{\alpha} + V_c\varepsilon_c^{\alpha} + V_a\varepsilon_a^{\alpha} + V_w\varepsilon_w^{\alpha} \tag{3}$$

where in (3):

α = geometric parameter
ε_r = relative bulk permittivity
V_{ag} = aggregate volume
V_c = cement volume
V_a = air-void volume
V_w = water volume
ε_{ag} = relative permittivity of aggregate (solid phase–matrix)
ε_c = relative permittivity of cement (solid phase–matrix)
ε_a = relative permittivity of air-void (gaseous phase–air)
ε_w = relative permittivity of water or moisture content (liquid phase–water)

It has been reported that the most common value used is α = 0.5 [73,74]. In some studies, the value of α = 0.46 is substituted and other studies have shown that α = 0.66 is more satisfactory for the research conducted [75]. Other work presented the shape factor to be α = 0.65 [76,77].

This paper is focused on finding the optimum α for modelling concrete mixtures. In order for the shape factor investigation to take place, all the material permittivities and volumetric properties were implemented in to the CRIM formula. In comparison with the simulated results (derived in the previous section), the error difference is plotted in Figure 5a with respect to α. The error with respect to the shape factor was calculated using 64 representative and realistic mixing models from the available training pool. As shown in Figure 5a, the error has minimised for a shape factor of $\alpha = 0.13$.

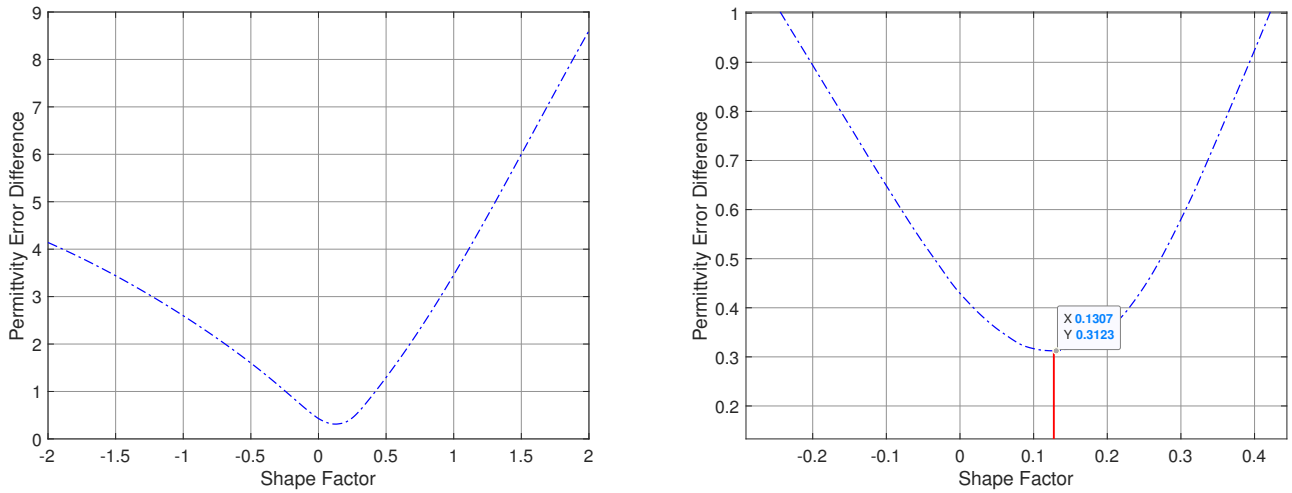

(**a**) (**b**)

Figure 5. The error betweenthe estimated permittivity using Finite-Difference Time-Domain (FDTD) and Complex Refractive Index Model (CRIM) models (**a**). Sub-figure (**b**), zooms in to better visualise the resulting shape factor.

To compare the results of this research with other mixing models such as the Rayleigh [29] and the Böttcher [30] models, the same calculation process was done.

The Rayleigh mixing model is presented as:

$$\frac{\varepsilon_{bulk} - \varepsilon_b}{\varepsilon_{bulk} + 2\varepsilon_b} = V_{sb}\frac{\varepsilon_s - \varepsilon_b}{\varepsilon_s + 2\varepsilon_b} + V_a\frac{\varepsilon_a - \varepsilon_b}{\varepsilon_a + 2\varepsilon_b} + V_{sw}\frac{\varepsilon_{sw} - \varepsilon_b}{\varepsilon_{sw} + 2\varepsilon_b} \tag{4}$$

The Böttcher mixing model is presented as:

$$\frac{\varepsilon_{bulk} - \varepsilon_b}{3\varepsilon_{bulk}} = V_{sb}\frac{\varepsilon_s - \varepsilon_b}{\varepsilon_s + 2\varepsilon_{bulk}} + V_a\frac{\varepsilon_a - \varepsilon_b}{\varepsilon_a + 2\varepsilon_{bulk}} + V_{sw}\frac{\varepsilon_{sw} - \varepsilon_b}{\varepsilon_{sw} + 2\varepsilon_{bulk}} \tag{5}$$

where in (4) and (5):

ε_{bulk} = bulk permittivity
ε_b = dielectric constant of binder
ε_s = dielectric constant of the solid phase (matrix)
ε_a = dielectric constant of the gaseous phase (air)
ε_{sw} = dielectric constant of the liquid phase (water)
V_{sb} = bulk volume of aggregate
V_a = volume of air
V_{sw} = volume of water

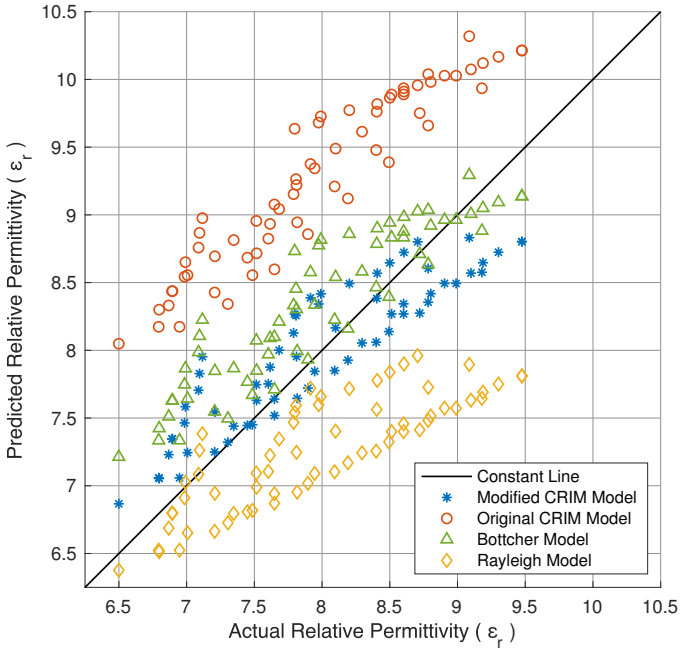

Figure 6. Comparison between different mixing models and the new modified CRIM model. The actual relative permittivity is based on the FDTD algorithm and the predicted relative permittivity is from the mixing models.

Equations (4) and (5) were used to calculate the bulk permittivity of the Rayleigh and the Böttcher models, respectively. By inserting the dielectric constant and the volume of each material, the formula calculates a specific bulk permittivity according to the given parameters. The Rayleigh mixing model has one output hence the permittivity calculation was simple. On the other hand, the Böttcher mixing models output was mathematically more complex. To overcome this time-consuming calculation, an automated procedure was programmed in MATLAB. A symbolic variable was created followed by a variable precision arithmetic (VPA) operation in order to derive four potential solutions. The positive solution was chosen as the bulk electric permittivity while the negative solutions were omitted.

Figure 6 illustrates the estimated permittivty using FDTD and the predicted permittivity using the aforementioned mixing models. It is apparent that the revised geometric factor performs better in comparison with the traditional CRIM model ($\alpha = 0.5$) and the other mixing models. This supports the premise that the revised CRIM using a shape factor of $\alpha = 0.13$ is a reliable mixing formula for predicting the bulk permittivity of concrete based on its aggregate, cement, water and air fraction content .

3. Laboratory Experiments

The revised shape factor was tested in laboratory experiments using a commercial horn antenna with 1 GHz central frequency. The experimental configuration is shown in Figure 7. The horn antenna was placed ≈40 cm above a concrete surface which consisted of 18 homogeneous and well-matured concrete blocks tightly packed. The concrete blocks were placed in a 6 × 3 grid format. The dimensions of each concrete block is 40 cm × 20 cm × 10 cm. The bulk permittivity of the concrete surface was evaluated based on equation [7]

$$\varepsilon = \left(\frac{1 + A_1/A_m}{1 - A_1/A_m} \right)^2 \tag{6}$$

where A_1 is the amplitude of the reflection from the concrete surface and A_m is the amplitude of the reflection when the concrete surface is covered with with a PEC plate [7]. A zero-offset correction was applied to each scan in an effort to remove static components that

might compromise the accuracy of the measurements. The bulk permittivity of the concrete blocks was estimated using (6) $\varepsilon_c \approx 7.8$. Subsequently, the gaps between the concrete blocks were gradually widened from 0–2-cm with 5 mm step in an effort to artificially increase the air-voids in a controlled manner and see the overall effects to the bulk permittivity. By increasing the gaps larger than 2 cm, it would act as voids rather than cracks hence the limited to 2 cm. Additionally, as the concrete blocks were homogeneous, the water fraction was consistent throughout the concrete block. Doing this, the bulk permittivity of the mixture concrete/air-voids could be evaluated with respect to the artificially created air-voids.

Since the permittivity of the concrete blocks was known ($\varepsilon_c \approx 7.8$), the bulk permittivity of the concrete/air-voids mixture could also be estimated using the CRIM model.

$$\varepsilon_b = ((1 - V_a)\varepsilon_c^{\alpha} + V_a\varepsilon_a^{\alpha})^{1/\alpha} \tag{7}$$

where ε_b is the CRIM-based bulk permittivity of the mixture concrete/air-voids, V_a is volumetric fraction of the artificially created air-voids, $\varepsilon_c \approx 7.8$ is the relative bulk permittivity of the concrete blocks, $\varepsilon_a = 1$ is the relative permittivity of free space and α is the shape factor. The revised shape factor $\alpha = 0.13$ and the default-one $\alpha = 0.5$ were used for the current example. The results are shown in Figure 8. The measured relative permittivity using (6) with respect to the artificially created air-gaps is illustrated with dots. The relative bulk permittivity estimated using CRIM (7) with $\alpha = 0.5$ and $\alpha = 0.13$ are illustrated with dotted and solid lines, respectively. It is apparent that the CRIM model using the optimised shape factor $\alpha = 0.13$ matched the measured bulk permittivity better and clearly over-performed the default $\alpha = 0.5$.

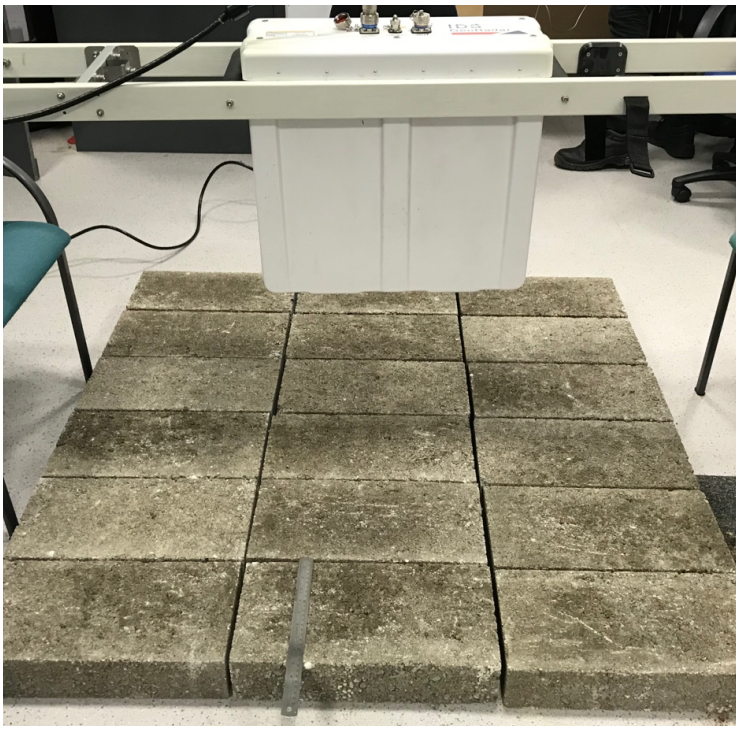

Figure 7. The experimental framework used to validate the revised shape factor. A horn antenna with 1 GHz central frequency is placed on top of a surface consisted of concrete blocks. The gaps between the concrete blocks are gradually increased in an effort to increase the overall volumetric fraction of air.

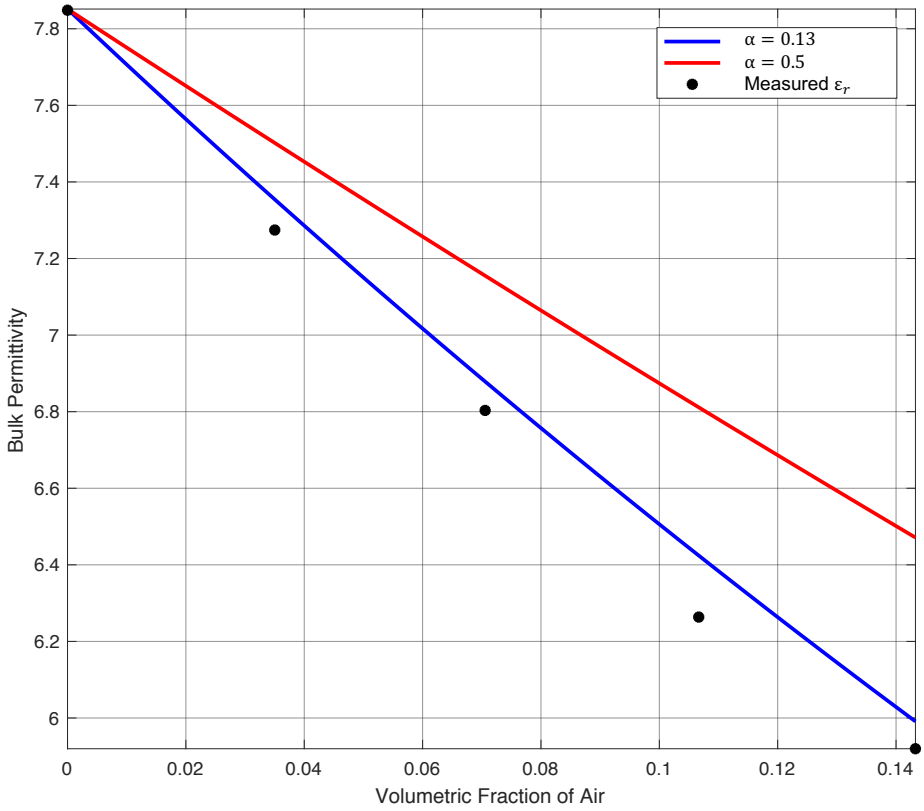

Figure 8. The measured and the calculated bulk permittivity using $\alpha = 0.5$ and $\alpha = 0.13$. It is apparent that the revised shape factor $\alpha = 0.13$ over-performs the default $\alpha = 0.5$.

4. Conclusions

An optimised shape factor for the CRIM mixing model has been obtained using realistic synthetic GPR models and verified by numerical experiments. The shape factor is fine-tuned for concrete applications and it is used to estimate the bulk permittivity of concrete based on its individual components (aggregates, cement, air voids and water fraction). The optimisation was done based on numerical simulations for a wide range of concrete samples with different properties and compositions. The concrete models were designed in 3D with a 1.5 GHz centre frequency GSSI-like antenna structure on the surface. The revised CRIM formula was in good agreement with the simulation results and clearly performed better compared to the default CRIM model. Subsequently, the modified CRIM was applied in a laboratory experiment in order to predict the effects of air voids to the bulk permittivity of concrete. The results using the numerically-derived shape factor were in good agreement with the laboratory measurements. Through numerical and laboratory measurements we have supported the premise that the proposed modified CRIM is a more reliable method for predicting the dielectric properties of concrete based on its components.

Author Contributions: Conceptualisation, H.Z., A.G. and I.G.; methodology, H.Z. and I.G.; execution, H.Z.; writing-review and editing, H.Z.; Proofreading, I.G. and A.G.; Supervision, A.G.; Project administration, A.G. All authors have read and agreed to the published version of the manuscript.

Funding: This research received no external funding.

Institutional Review Board Statement: Not applicable.

Informed Consent Statement: Not applicable.

Data Availability Statement: The data used in this research are available from the authors upon reasonable requests.

Conflicts of Interest: The authors declare that there are no conflicts of interest.

References

1. Daniels, D.J. *Ground Penetrating Radar*, 2nd ed.; The University of Michigan: London, UK, 2005.
2. Jol, H.M. *Ground pEnetrating Radar Theory and Applications*; Elsevier: Amsterdam, The Netherlands, 2008.
3. Annan, A. Ground-penetrating radar. In *Near-Surface Geophysics*; Society of Exploration Geophysicists: Tulsa, Oklahoma, 2005; pp. 357–438.
4. El-Mahallawy, M.S.; Hashim, M. Material classification of underground utilities from GPR images using DCT-based SVM approach. *IEEE Geosci. Remote Sens. Lett.* **2013**, *10*, 1542–1546. [CrossRef]
5. Gabryś, M.; Kryszyn, K.; Ortyl, Ł. GPR surveying method as a tool for geodetic verification of GESUT database of utilities in the light of BSI PAS128. *Rep. Geod. Geoinform.* **2019**, *107*, 49–59.
6. Kang, M.S.; Kim, N.; Im, S.B.; Lee, J.J.; An, Y.K. 3D GPR Image-based UcNet for Enhancing Underground Cavity Detectability. *Remote Sens.* **2019**, *11*, 2545. [CrossRef]
7. Saarenketo, T.; Scullion, T. Road evaluation with ground penetrating radar. *J. Appl. Geophys.* **2000**, *43*, 119–138. [CrossRef]
8. Cardarelli, E.; Marrone, C.; Orlando, L. Evaluation of tunnel stability using integrated geophysical methods. *J. Appl. Geophys.* **2003**, *52*, 93–102. [CrossRef]
9. Hugenschmidt, J. Concrete bridge inspection with a mobile GPR system. *Constr. Build. Mater.* **2002**, *16*, 147–154. [CrossRef]
10. Hugenschmidt, J.; Mastrangelo, R. GPR inspection of concrete bridges. *Cem. Concr. Compos.* **2006**, *28*, 384–392. [CrossRef]
11. Diamanti, N.; Annan, A.P.; Redman, J.D. Concrete bridge deck deterioration assessment using ground penetrating radar (GPR). *J. Environ. Eng. Geophys.* **2017**, *22*, 121–132. [CrossRef]
12. Maierhofer, C. Nondestructive evaluation of concrete infrastructure with ground penetrating radar. *J. Mater. Civ. Eng.* **2003**, *15*, 287–297. [CrossRef]
13. Xie, X.; Li, P.; Qin, H.; Liu, L.; Nobes, D.C. GPR identification of voids inside concrete based on the support vector machine algorithm. *J. Geophys. Eng.* **2013**, *10*, 034002. [CrossRef]
14. Giannakis, I.; Giannopoulos, A.; Davidson, N. Realistic modelling of ground penetrating radar for landmine detection using FDTD. In Proceedings of the 15th International Conference on Ground Penetrating Radar, Brussels, Belgium, 30 June–4 July 2014; pp. 954–959.
15. Chang, C.W.; Lin, C.H.; Lien, H.S. Measurement radius of reinforcing steel bar in concrete using digital image GPR. *Constr. Build. Mater.* **2009**, *23*, 1057–1063. [CrossRef]
16. Mai, T.C.; Razafindratsima, S.; Sbartaï, Z.M.; Demontoux, F.; Bos, F. Non-destructive evaluation of moisture content of wood material at GPR frequency. *Constr. Build. Mater.* **2015**, *77*, 213–217. [CrossRef]
17. Hoegh, K.; Khazanovich, L.; Dai, S.; Yu, T. Evaluating asphalt concrete air void variation via GPR antenna array data. *Case Stud. Nondestr. Test. Eval.* **2015**, *3*, 27–33. [CrossRef]
18. Shang, J.Q. Effects of asphalt pavement properties on complex permittivity. *Int. J. Pavement Eng.* **2002**, *3*, 217–226. [CrossRef]
19. Pérez-Gracia, V.; García, F.G.; Abad, I.R. GPR evaluation of the damage found in the reinforced concrete base of a block of flats: A case study. *NDT e Int.* **2008**, *41*, 341–353. [CrossRef]
20. Klysz, G.; Balayssac, J.; Ferrières, X. Evaluation of dielectric properties of concrete by a numerical FDTD model of a GPR coupled antenna—parametric study. *NDT e Int.* **2008**, *41*, 621–631. [CrossRef]
21. Tsui, F.; Matthews, S. Analytical modelling of the dielectric properties of concrete for subsurface radar applications. *Constr. Build. Mater.* **1997**, *11*, 149–161. [CrossRef]
22. Bourdi, T.; Rhazi, J.E.; Boone, F.; Ballivy, G. Application of Jonscher model for the characterization of the dielectric permittivity of concrete. *J. Phys. D Appl. Phys.* **2008**, *41*, 205410. [CrossRef]
23. Bourdi, T.; Rhazi, J.E.; Boone, F.; Ballivy, G. Modelling dielectric-constant values of concrete: An aid to shielding effectiveness prediction and ground-penetrating radar wave technique interpretation. *J. Phys. D Appl. Phys.* **2012**, *45*, 405401. [CrossRef]
24. Redman, J.D.; Annan, A.P.; Diamanti, N. Measurement of bulk electrical properties using GPR with a variable reflector. *J. Environ. Eng. Geophys.* **2018**, *23*, 489–496. [CrossRef]
25. Böttcher, C.J.F. *Theory Electric Polarisation*; Elsevier Publishing Company: Amsterdam, The Netherlands, 1952.
26. Sihvola, A.H. *Electromagnetic Mixing Formulas and Applications*; IET Digital Library: Padstow, UK, 1999.
27. Al-Qadi, I.L.; Leng, Z.; Lahouar, S.; Baek, J. In-place hot-mix asphalt density estimation using ground-penetrating radar. *Transp. Res. Rec.* **2010**, *2152*, 19–27. [CrossRef]
28. Birchak, J.R.; Gardner, C.G.; Hipp, J.E.; Victor, J.M. High dielectric constant microwave probes for sensing soil moisture. *Proc. IEEE* **1974**, *62*, 93–98. [CrossRef]
29. Rayleigh, L. LVI. On the influence of obstacles arranged in rectangular order upon the properties of a medium. *Lond. Edinb. Dublin Philos. Mag. J. Sci.* **1892**, *34*, 481–502. [CrossRef]
30. Böttcher, C.J.F.; van Belle, O.C.; Bordewijk, P.; Rip, A. *Theor. electr. Polarization*; Elsevier Science Ltd: Amsterdam, The Netherlands, 1978.
31. Brown, W.F.; Franz, W.; Forsbergh, P. Dielectrics/Dielektrika. *Handbuch der Physik*; Springer: Heidelberg, Germany, 1956.
32. Wagner, A. Physik, 40, 817 (1913). *Arch. Elektroteeh* **1914**, *3*, 83.
33. Bruggeman, V.D. Berechnung verschiedener physikalischer Konstanten von heterogenen Substanzen. I. Dielektrizitätskonstanten und Leitfähigkeiten der Mischkörper aus isotropen Substanzen. *Annalen der physik* **1935**, *416*, 636–664. [CrossRef]

34. Topp, G.C.; Davis, J.L.; Annan, A.P. Electromagnetic determination of soil water content: Measurements in coaxial transmission lines. *Water Resour. Res.* **1980**, *16*, 574–582. [CrossRef]
35. Warren, C.; Giannopoulos, A.; Giannakis, I. gprMax: Open source software to simulate electromagnetic wave propagation for Ground Penetrating Radar. *Comput. Phys. Commun.* **2016**, *209*, 163–170. [CrossRef]
36. Warren, C.; Giannopoulos, A.; Gray, A.; Giannakis, I.; Patterson, A.; Wetter, L.; Hamrah, A. A CUDA-based GPU engine for gprMax: open source FDTD electromagnetic simulation software. *Comput. Phys. Commun.* **2019**, *237*, 208–218. [CrossRef]
37. Taflove, A.; Hagness, S.C. *Computational Electromagnetics: The Finite-Difference Time-Domain Method*, 3rd ed.; Artech House Publishers: London, UK, 2005.
38. Yee, K. Numerical solution of initial boundary value problems involving Maxwell's equations in isotropic media. *IEEE Trans. Antennas Propag.* **1966**, *14*, 302–307.
39. Sadiku, M.N. *Numerical Techniques in Electromagnetics*; CRC press: Boca Raton, FL, USA, 2000.
40. Cassidy, N.J. A review of practical numerical modelling methods for the advanced interpretation of ground-penetrating radar in near-surface environments. *Near Sur. Geophys.* **2007**, *5*, 5–21. [CrossRef]
41. Cassidy, N.J.; Millington, T.M. The application of finite-difference time-domain modelling for the assessment of GPR in magnetically lossy materials. *J. Appl. Geophys.* **2009**, *67*, 296–308. [CrossRef]
42. Giannakis, I.; Giannopoulos, A.; Warren, C. A realistic FDTD numerical modeling framework of ground penetrating radar for landmine detection. *IEEE J. Sel. Top. Appl. Earth Obs. Remote Sens.* **2016**, *9*, 37–51. [CrossRef]
43. Lee, K.H.; Chen, C.C.; Teixeira, F.L.; Lee, R. Modeling and investigation of a geometrically complex UWB GPR antenna using FDTD. *IEEE Trans. Antennas Propag.* **2004**, *52*, 1983–1991. [CrossRef]
44. Uduwawala, D. Modeling and investigation of planar parabolic dipoles for GPR applications: A comparison with bow-tie using FDTD. *J. Electomagn. Waves Appl.* **2006**, *20*, 227–236. [CrossRef]
45. Giannakis, I.; Giannopoulos, A.; Warren, C. Realistic FDTD GPR antenna models optimized using a novel linear/nonlinear Full-Waveform Inversion. *IEEE Trans. Geosci. Remote Sens.* **2019**, *57*, 1768–1778. [CrossRef]
46. Bourgeois, J.M.; Smith, G.S. A fully three-dimensional simulation of a ground-penetrating radar: FDTD theory compared with experiment. *IEEE Trans. Geosci. Remote Sens.* **1996**, *34*, 36–44. [CrossRef]
47. Klysz, G.; Balayssac, J.; Laurens, S.; Ferrieres, X. Numerical FDTD simulation of the direct wave propagation of a GPR coupled antenna. In Proceedings of the Tenth International Conference on Grounds Penetrating Radar, Delft, The Netherlands, 21–24 June 2004; pp. 45–48.
48. Caratelli, D.; Yarovoy, A.; Ligthart, L.P. Accurate FDTD modelling of resistively-loaded bow-tie antennas for GPR applications. In Proceedings of the 2009 3rd European Conference on Antennas and Propagation, Berlin, Germany, 23–27 March 2009; pp. 2115–2118.
49. Bourgeois, J.; Smith, G. A complete electromagnetic simulation of a ground penetrating radar for mine detection: Theory and experiment. In Proceedings of the IEEE Antennas and Propagation Society International Symposium 1997, Montreal, QC, Canada, 13–18 July 1997; pp. 986–989.
50. Radzevicius, S.J.; Chen, C.C.; Peters Jr, L.; Daniels, J.J. Near-field dipole radiation dynamics through FDTD modeling. *J. Appl. Geophys.* **2003**, *52*, 75–91. [CrossRef]
51. Diamanti, N.; Annan, A.P. Characterizing the energy distribution around GPR antennas. *J. Appl. Geophys.* **2013**, *99*, 83–90. [CrossRef]
52. Lampe, B.; Holliger, K. Resistively loaded antennas for ground-penetrating radar: A modeling approach. *Geophysics* **2005**, *70*, K23–K32. [CrossRef]
53. Venkatarayalu, N.V.; Chen, C.C.; Teixeira, F.L.; Lee, R. Numerical modeling of ultrawide-band dielectric horn antennas using FDTD. *IEEE Trans. Antennas Propag.* **2004**, *52*, 1318–1323. [CrossRef]
54. Turk, A.S.; Sahinkaya, D.A.; Sezgin, M.; Nazli, H. Investigation of convenient antenna designs for ultra-wide band GPR systems. In Proceedings of the 2007 4th International Workshop on, Advanced Ground Penetrating Radar, Aula Magna Partenope, Italy, 27–29 June 2007; pp. 192–196.
55. Warren, C.; Giannopoulos, A. Creating finite-difference time-domain models of commercial ground-penetrating radar antennas using Taguchi's optimization method. *Geophysics* **2011**, *76*, G37–G47. [CrossRef]
56. Robert, A. Dielectric permittivity of concrete between 50 MHz and 1 GHz and GPR measurements for building materials evaluation. *J. Appl. Geophys.* **1998**, *40*, 89–94. [CrossRef]
57. Al-Saleh, S.A. Analysis of total chloride content in concrete. *Case Stu. Constr. Mater.* **2015**, *3*, 78–82. [CrossRef]
58. Laurens, S.; Balayssac, J.; Rhazi, J.; Klysz, G.; Arliguie, G. Non-destructive evaluation of concrete moisture by GPR: experimental study and direct modeling. *Mater. Struct.* **2005**, *38*, 827–832. [CrossRef]
59. Wu, Z.; Wong, H.; Buenfeld, N. Transport properties of concrete after drying-wetting regimes to elucidate the effects of moisture content, hysteresis and microcracking. *Cem. Concr. Res.* **2017**, *98*, 136–154. [CrossRef]
60. Shaw, M. The permittivity and conductivity of concretes at ground-penetrating radar frequencies. *Adv. Cem. Res.* **1998**, *10*, 187–194. [CrossRef]
61. Soutsos, M.; Bungey, J.; Millard, S.; Shaw, M.; Patterson, A. Dielectric properties of concrete and their influence on radar testing. *NDT e Int.* **2001**, *34*, 419–425. [CrossRef]

62. Terrasse, G.; Nicolas, J.M.; Trouvé, E.; Drouet, É. Automatic localization of gas pipes from GPR imagery. In Proceedings of the 2016 24th European Signal Processing Conference (EUSIPCO), Budapest, Hungary, 29 August–2 September 2016; pp. 2395–2399.
63. Daniels, D.J. A review of GPR for landmine detection. *Sens. Imaging Int. J.* **2006**, *7*, 90–123. [CrossRef]
64. Brown, E. Density of asphalt concrete-how much is needed? In Proceedings of the 69th Annual Meeting of the TransportationResearch Board, Washington, DC, USA, 8–9 January 1990.
65. Yelf, R. Where is true time zero? In Proceedings of the Tenth International Conference on Grounds Penetrating Radar, Delft, The Netherlands, 21–24 June 2004; pp. 279–282.
66. Zadhoush, H. Numerical modelling of ground penetrating radar for optimisation of the time-zero adjustment and complex refractive index model. Ph.D. Thesis, The University of Edinburgh, Edinburgh, UK, 2020.
67. Warren, C.; Giannopoulos, A. Investigation of the directivity of a commercial ground-penetrating radar antenna using a finite-difference time-domain antenna model. In Proceedings of the 2012 14th International Conference on Ground Penetrating Radar (GPR), Shanghai, China, 4–8 June 2012; pp. 226–231.
68. Ahrens, J.; Geveci, B.; Law, C. Paraview: An end-user tool for large data visualization. *Vis. Handb.* **2005**, *717*, 8.
69. Lachowicz, J.; Rucka, M. A concept of heterogeneous numerical model of concrete for GPR simulations. In Proceedings of the 2017 9th International Workshop on Advanced Ground Penetrating Radar (IWAGPR), Edinburgh, UK, 28–30 June 2017; pp. 1–4.
70. Grassl, P.; Wong, H.S.; Buenfeld, N.R. Influence of aggregate size and volume fraction on shrinkage induced micro-cracking of concrete and mortar. *Cem. Concr. Res.* **2010**, *40*, 85–93. [CrossRef]
71. Kemper, W.; Rosenau, R. Aggregate stability and size distribution. *Methods Soil Anal. Part I Phys. Mineral. Methods* **1986**, *5*, 425–442.
72. Jury, W.A.; Horton, R. *Soil Physics*; John Wiley & Sons: Hoboken, NJ, USA, 2004.
73. Ukaegbu, I.K.; Gamage, K.A.; Aspinall, M.D. Nonintrusive Depth Estimation of Buried Radioactive Wastes Using Ground Penetrating Radar and a Gamma Ray Detector. *Remote Sens.* **2019**, *11*, 141. [CrossRef]
74. Roth, K.; Schulin, R.; Flühler, H.; Attinger, W. Calibration of time domain reflectometry for water content measurement using a composite dielectric approach. *Water Resour. Res.* **1990**, *26*, 2267–2273. [CrossRef]
75. Gardner, C.; Dean, T.; Cooper, J. Soil water content measurement with a high-frequency capacitance sensor. *J. Agric. Eng. Res.* **1998**, *71*, 395–403. [CrossRef]
76. Dobson, M.C.; Ulaby, F.T.; Hallikainen, M.T.; El-Rayes, M.A. Microwave dielectric behavior of wet soil-Part II: Dielectric mixing models. *IEEE Trans. Geosci. Remote Sens.* **1985**, *GE-23*, 35–46. [CrossRef]
77. Peplinski, N.R.; Ulaby, F.T.; Dobson, M.C. Dielectric properties of soils in the 0.3-1.3-GHz range. *IEEE Trans. Geosci. Remote Sens.* **1995**, *33*, 803–807. [CrossRef]